Acta metall. mater. Vol. 39, No. 8, pp. 1871–1882, 1991
Printed in Great Britain. All rights reserved

0956-7151/91 $3.00 + 0.00
Copyright © 1991 Pergamon Press plc

PARTICLE REINFORCEMENT OF DUCTILE MATRICES AGAINST PLASTIC FLOW AND CREEP

G. BAO,[1] J. W. HUTCHINSON[2] and R. M. McMEEKING[3]

[1]Materials Department, University of California, Santa Barbara, CA 93106, [2]Division of Applied Sciences, Harvard University, Cambridge, MA 02138 and [3]Materials Department and Mechanical Engineering Department, University of California, Santa Barbara, CA 93106, U.S.A.

(Received 19 July 1990; in revised form 24 December 1990)

Abstract—A theoretical investigation is made of the role of non-deforming particles in reinforcing ductile matrix materials against plastic flow and creep. The study is carried out within the framework of continuum plasticity theory using cell models to implement most of the calculations. Systematic results are given for the influence of particle volume fraction and shape on the overall behavior of composites with uniformly distributed, aligned reinforcement. The stress–strain behavior of the matrix material is characterized by elastic–perfectly plastic behavior or by power-law hardening behavior of the Ramberg–Osgood type. A relatively simple connection is noted between the asymptotic reference stress for the composite with the power-law hardening matrix and the limit flow stress of the corresponding composite with the elastic–perfectly plastic matrix. The asymptotic reference stress for the composite with the power-law matrix is applicable to steady-state creep. A limited study is reported on the overall limit flow stress for composites with randomly orientated disc-like or needle-like particles when the particles are arranged in a packet-like morphology.

Résumé—Nous avons étudié théoriquement le rôle des particules indéformables dans l'amélioration de la tenue des matériaux à matrice ductile *vis-à-vis* de la déformation plastique et du fluage. Cette étude a été menée dans le cadre de la théorie plastique des milieux continus, en utilisant des modèles de cellules pour exécuter la plupart des calculs. Nous donnons des résultats systématiques concernant l'influence de la fraction volumique et de la forme des particules sur le comportement général des composites à renforts alignés et distribués de façon uniforme. La loi contrainte–déformation de la matrice est caractérisée par un comportement élastique–plastique parfait, ou par un comportement de consolidation en loi de puissance du type de Ramberg et Osgood. On note une relation relativement simple entre la contrainte de référence asymptotique correspondant au composite dont la matrice présente une consolidation en loi de puissance, et la contrainte d'écoulement limite du composite correspondant dont la matrice est élastique–parfaitement plastique. La contrainte asymptotique de référence du premier composite est applicable au fluage stationnaire. Nous rapportons une étude moins détaillée sur la contrainte globale d'écoulement limite dans le cas des composites aù les particules en forme de disques ou d'aiguilles sont orientées au hasard, alors que leur arrangement présente une morphologie en paquets.

Zusammenfassung—Die rolle sich nicht verformender Teilchen bei der Härtung duktiler Matrixmaterialien gegen plastiches Fließen und Kriechen wird theoretisch untersucht. Die meisten Rechnungen werden mit Zellmodellen im Rahmen der Kontinuums–Plastizitätstheorie durchgeführt. Systematische Ergebnisse werden vorgelegt für den Einfluß des Teilchen-Volumanteils und der Teilchenform auf das Verhalten des Verbundwerkstoffes bei gleichmäßig verteilten ausgerichteten Verstärkungsteilchen. Das Spannungs-Dehnungsverhalten des Matrixmaterials ist charakterisiert durch elastisch-perfektes plastisches Verhalten oder durch Potenzgesetz–Härtungsverhalten vom Typ Ramberg–Osgood. Zwischen der asymptotischen Referenzspannung des Verbundmateriales mit der potenzgesetzverfestigenden Matrix und der Grenzfließspannung des entsprechenden Verbundmaterials mit der elastisch–perfekt plastischen Matrix ergibt sich ein vergleichsweise einfacher Zusammenhang. Die asymptotische Vergleichsspannung für den Verbundwerkstoff mit der Potenzgesetz-Matrix läßt sich auf das stationäre Kriechen anwenden. Eine kurze Untersuchung der Grenzfließspannung von Verbundmaterialien mit willkürlich orientierten scheibenförmigen oder nadelartigen Teilchen wird für den Fall dargestellt, daß die Teilchen paketartig angeordnet sind.

1. INTRODUCTION

Composites comprised of a metal or intermetallic matrix reinforced by particles or fibers which do not deform plastically have properties which make them potentially attractive for a range of applications, including high specific stiffness materials and creep resistant high temperature materials. This paper is concerned with the uniaxial stress–strain behavior in rate-independent plastic flow or in steady-state creep for composites with matrices reinforced by particles which are large enough to justify a continuum plasticity representation of the matrix behavior. In particular, an attempt has been made to present results which systematically relate the overall response of the composite to the particle volume fraction, particle shape, and matrix strain hardening. For the most part, attention is focussed on aligned particles, but

some results are given for composites with randomly orientated needle- or disc-shaped particles.

Since the theory for determining the overall elastic properties of two-phase composites is relatively well developed, the emphasis here is on nonlinear plastic response. Two recent publications [1,2] complement the present study and provide surveys of the relevant literature. The issue of whether a continuum theory of plasticity is appropriate to characterize the matrix material for a given size of reinforcing particle has received attention but remains open, as will be discussed further in the final section (the recent literature on the subject is cited in [2]).

The features of the overall stress–strain behavior which will be of concern in this study are brought out in Fig. 1. The tensile stress–strain curve of an elastic–perfectly plastic matrix material in Fig. 1(a) is characterized by

$$\sigma = \sigma_0(\epsilon/\epsilon_0) \qquad \epsilon \leqslant \epsilon_0$$
$$= \sigma_0 \qquad \epsilon > \epsilon_0 \tag{1}$$

where σ_0 is the tensile flow stress, $\epsilon_0 = \sigma_0/E$, and E is Young's modulus. A composite with non-deforming, perfectly bonded particles embedded in a perfectly-plastic matrix will have a limit flow stress $\bar{\sigma}_0$ for tensile stressing in any given direction. With the exception of Sections 6 and 7 of the paper, attention will be focussed on particles which are aligned with respect to the tensile axis, and the limit flow stress $\bar{\sigma}_0$ will be with reference to that specific direction of stressing. Sections 2, 3 and 4 deal with the relation between $\bar{\sigma}_0$ and the volume fraction and shape of the particles.

Section 5 is concerned with matrices which strain harden. Because of the close connection between power law hardening and steady-state power law creep, the results of Section 5 are also applicable to reinforcement against creep by rigid particles. The tensile stress–strain behavior for the hardening matrix used in this paper is the Ramberg–Osgood [3] curve

$$\epsilon = \frac{\sigma}{E} + \alpha\frac{\sigma_0}{E}\left(\frac{\sigma}{\sigma_0}\right)^n \tag{2a}$$

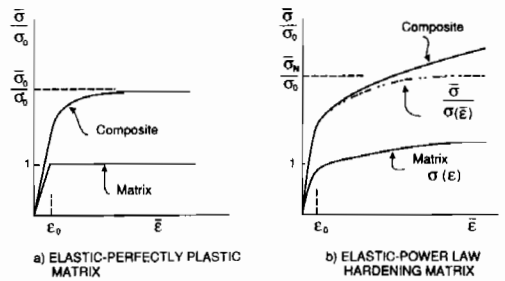

Fig. 1. Tensile stress–strain curves for composite and matrix defining the limit flow stress $\bar{\sigma}_0$ in (a) and the asymptotic reference stress $\bar{\sigma}_N$ in (b).

or

$$\frac{\epsilon}{\epsilon_0} = \frac{\sigma}{\sigma_0} + \alpha\left(\frac{\sigma}{\sigma_0}\right)^n \tag{2b}$$

where n is the stress exponent, $\epsilon_0 = \sigma_0/E$, and the coefficient α is taken to be 3/7 by Ramberg and Osgood. The overall tensile stress–strain behavior of the composite [see Fig. 1(b)] with perfectly bonded particles necessarily has the same stress hardening exponent n for overall strains $\bar{\epsilon}$ which are sufficiently large compared to ϵ_0. That is, the overall (or average) tensile stress–strain curve for sufficiently large $\bar{\epsilon}$ asymptotes to

$$\frac{\bar{\epsilon}}{\epsilon_0} = \alpha\left(\frac{\bar{\sigma}}{\bar{\sigma}_N}\right)^n \quad \text{or} \quad \frac{\bar{\sigma}}{\bar{\sigma}_N} = \left(\frac{\bar{\epsilon}}{\alpha\epsilon_0}\right)^N \tag{3}$$

where $N = 1/n$ is the strain hardening exponent and $\bar{\sigma}_N$ will be called the asymptotic reference stress. This property is an exact consequence of the Il'yushin Theorem for pure power law materials.

Because the Ramberg–Osgood law (2) approaches the elastic–perfectly plastic law (1) as $n \to \infty$

$$\lim_{N \to O} \bar{\sigma}_N = \bar{\sigma}_0. \tag{4}$$

Thus, $\bar{\sigma}_0$ reflects the reinforcement even for a hardening matrix and $\bar{\sigma}_0$ is the premiere quantity from a continuum theory for assessing reinforcement. A simple approximate formula relating $\bar{\sigma}_N$ to $\bar{\sigma}_0$ will be quoted in Section 5.

A straightforward way to reveal the asymptotic reference stress is to plot the composite stress $\bar{\sigma}$ normalized by the stress in the pure matrix material at the same strain $\bar{\epsilon}$, as depicted by the dashed curve in Fig. 1(b). Specifically, let $\sigma(\epsilon)$ denote (2) and plot $\bar{\sigma}(\bar{\epsilon})/\sigma(\bar{\epsilon})$.

The results of Section 5 have bearing on matrices which undergo steady-state creep which is characterized in simple tension by

$$\dot{\epsilon}/\dot{\epsilon}_0 = \alpha(\sigma/\sigma_0)^n \tag{5}$$

where $\dot{\epsilon}_0$ is a reference strain-rate and σ_0 a reference stress. The composite has a steady-state creep behavior given by

$$\dot{\bar{\epsilon}}/\dot{\epsilon}_0 = \alpha(\bar{\sigma}/\bar{\sigma}_N)^n \tag{6}$$

where $\bar{\sigma}_N/\sigma_0$ has the same value as for the rate-independent power hardening material for a given reinforcement. The analog between power law plasticity and power law creep implied by (3), (5) and (6) is exact, following from the Il'yushin Theorem cited above. The *transition* to steady-state creep, or the *transition* to power-law behavior (3) for the rate-independent material, may require strains that are as much as 10 times ϵ_0. This is an important aspect of the macroscopic response of heavily reinforced materials which will be discussed in the body of the paper.

Most of the results in this paper are based on an axisymmetric cell model of a uniform, aligned particle

distribution. Axisymmetric cell models have been widely used for this purpose [1, 4, 5]. The scheme behind the cell model is illustrated in Fig. 2. Imagine, for example, a hexagonal array of axisymmetric particles aligned with the hexagonal cells and subject to an overall stress $\bar{\sigma}$ parallel to the hexagonal axis. Each hexagonal cell behaves identically. The lateral faces remain planar with zero shear traction and zero average normal traction. The faces perpendicular to the direction of stressing also remain planar with zero shear tractions and with average normal stress equal to $\bar{\sigma}$. The cylindrical cell is introduced as an approximation to the hexagonal cell for computational reasons—the stress distribution is axisymmetric if the particle is axisymmetric. The cylindrical surface of the cell is constrained to remain cylindrical but is free to move out or in with zero average normal tractions. The shear tractions on the cylindrical sides and the ends are zero. The average normal stress on the ends is $\bar{\sigma}$. The volume fraction of the particles, f, is taken as the ratio of the particle volume to the cell volume. The cell model is an approximation to a uniform distribution of aligned particles with an arrangement such as that illustrated in Fig. 2. Results for high aspect ratio particles are particularly sensitive to other arrangements, as will be remarked on below.

A finite element method has been used to solve the boundary value problems for the axisymmetric cell. The ABAQUS code was employed with 8-noded biquadratic elements. In generating results over the full range of volume fractions, calculations at as many as 6 distinct values of f were made. Convergence studies were conducted at representative volume fractions, both small and large, to ensure that the element meshes were sufficiently refined. The overall stress–strain curves discussed below were computed incrementally using strain increments which were equal to or less than $\Delta\bar{\epsilon}/\epsilon_0 = 0.25$. Thus, as many as 40 incremental steps were taken to calculate each curve for strains up to $10\,\epsilon_0$. However, in the transition from elastic behavior to yielding, steps as small as $\Delta\bar{\epsilon}/\epsilon_0 = 0.03$ were used to ensure fidelity to a tolerance criterion for convergence of the incremental solution. In any case, the fully plastic flow which eventually develops is insensitive to the initial transient calculation leading to it. The results in Section 6 were obtained using a 3-D cell, and some details of the finite element scheme used in those calculations will be given later.

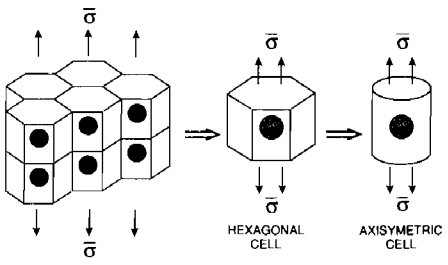

Fig. 2. Motivation for axisymmetric cell model.

The J_2 flow theory of plasticity is used to characterize the rate-independent matrix material. With s_{ij} as the stress deviator and $\sigma_e = (3\,s_{ij}s_{ij}/2)^{1/2}$ as the effective stress, the stress increment is related to the strain increment by the well-known flow theory formula

$$\dot{\sigma}_{ij} = \frac{E}{1+\nu}\left\{\dot{\epsilon}_{ij} + \frac{\nu}{1-2\nu}\dot{\epsilon}_{kk}\delta_{ij} - \frac{3}{2}\frac{(1+\nu)\sigma_e^{-2}s_{ij}s_{kl}\dot{\epsilon}_{kl}}{[1+\frac{2}{3}(1+\nu)(E/E_t - 1)^{-1}]}\right\} \quad (7)$$

where E is Young's modulus, ν is Poisson's ratio, and E_t is the tangent modulus of the tensile stress–strain curve at the current value of σ_e. The last term in (7) is taken to be zero for an elastic increment. In all the calculations, ν was taken to be 0.25; however, the quantities of primary interest, $\bar{\sigma}_0$ and $\bar{\sigma}_N$, are independent of ν. No calculations were carried out for steady-state creep, but the correspondence noted between $\bar{\sigma}_N$ for the rate-independent theory and $\bar{\sigma}_N$ for steady-state creep holds when (5) is generalized to multiaxial states by

$$\dot{\epsilon}_{ij}/\dot{\epsilon}_0 = (3/2)\,\alpha(\sigma_e/\sigma_0)^{n-1}s_{ij}/\sigma_0. \quad (8)$$

The particles are taken to be rigid and the matrix material is taken to be perfectly bonded to the particles. The elasticity of the particles affects the overall elastic modulus of the composite, $\bar{E}$, and to a minor extent affects the overall stress–strain curve of the composite in the vicinity of overall yeield. However, as long as the particles do not yield themselves, their elasticity has no influence on $\bar{\sigma}_0$ nor $\bar{\sigma}_N$. Since the emphasis in this work is on the plastic behavior of the composites, it was expedient to take the particles to be rigid and thereby eliminate the ratio of the modulus of the particle to that of the matrix as an additional parameter. Various methods for estimating the overall elastic moduli of reinforced solids are available which account for the elasticity of the particles [6]. These estimates can be incorporated in the approximate representation of the full stress–strain curve for composites proposed in Section 5.

2. ELASTIC–PERFECTLY PLASTIC MATRIX REINFORCED BY RIGID SPHERES

Stress–strain curves for the elastic-perfectly plastic matrix and for the matrix containing rigid spherical particles, as calculated using the cylindrical cell model, are shown in Fig. 3. In all cases presented in this section the aspect ratio of the cell, R/H, is fixed at unity. The Influence of the cell aspect ratio is discussed in the next section. A uniform distribution of spherical particles has surprisingly little effect on the overall flow stress for volume fractions below 0.2. This is remarkable considering that the distance

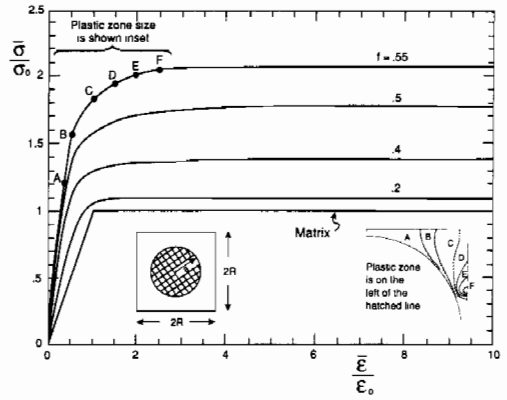

Fig. 3. Uniaxial stress–strain curves for an elastic–perfectly plastic matrix containing a uniform array of rigid spherical particles. The aspect ratio of the cell was taken to be unity.

between particles is about the diameter of the particles when $f = 0.1$.

The strain required for the composite to make the transition from elastic to perfectly plastic with $d\bar{\sigma}/d\bar{\epsilon} = 0$ increases as the level of reinforcement increases. At the highest levels of reinforcement in Fig. 3, the transition strain is about $3\,\epsilon_0$.

The dependence of $\bar{\sigma}_0/\sigma_0$ on f is shown in Fig. 4(a). The composite flow stress becomes unbounded when the particles come into contact, which occurs at $f = 2/3$ when the cell aspect ratio is unity. Included in Fig. 4(a) are three points from Hom and McMeeking [7] computed using a three-dimensional cell model of a uniform cubic array of rigid spherical particles in an elastic–perfectly plastic matrix. The tensile axis is aligned with an axis of the cubical cell. The coincidence of the two sets of results suggests that the composite flow stress is not very sensitive to the precise arrangement of the spherical particles for volume fractions up to 0.4 as long as the distribution is uniform and arranged in a primitive manner. Also included in Fig. 4(a) is the prediction from a self-consistent model for reinforcement by rigid spherical particles due to Duva [8]. Duva's model will be discussed in Section 5; in the limit of perfect plasticity it gives

$$\bar{\sigma}_0/\sigma_0 = (1-f)^{-0.39}. \tag{9}$$

It is insightful to express the composite flow stress as

$$\bar{\sigma}_0/\sigma_0 = 1 + \beta f. \tag{10}$$

The reinforcement factor β is plotted in Fig. 4(b). For sufficiently small f the increase in composite flow stress must be approximately linear in f (i.e. $\beta \to \beta_0$ as $f \to 0$). This is the dilute limit. Figure 4(b) reveals that the dilute range for spherical particles extends to volume fractions as large as $f = 0.2$. Duva's model is constructed to be exact in the dilute limit, as discussed in Section 5; but compared to the present predictions and those of [7] it underestimates the reinforcement at particle volume fractions above 0.2.

In the dilute limit the axisymmetric cell model for rigid spherical particles gives

$$\beta = 0.375. \tag{11}$$

Considerable care has been exercised to validate the accuracy of this value by various refinements of the finite element mesh. The major uncertainty in the value (11) arises from the fact that the circular cylinder cell is not space-filling. If the volume of the cell is taken to be that of the hexagonal cell which ascribes the circular cylindrical cell, rather than that of the cylindrical cell itself, the volume fraction f increases by a factor $2\pi/(3\sqrt{3}) = 1.21$ and β becomes 0.310. If, on the other hand, the volume of the cell is taken to be that of the circumscribing hexagonal cell, f must be decreased by the factor $\pi/\sqrt{12} = 0.907$ and β becomes 0.413. Such uncertainties are intrinsic to an axisymmetric cell model. An independent calculation, discussed in Section 5, which is free of this uncertainty gives $\beta = 0.39$. Thus, it appears that the identification of the cell volume with that of the circular cylinder is an appropriate choice to determine f, at least when f is small, and we shall continue to make this identification throughout the paper.

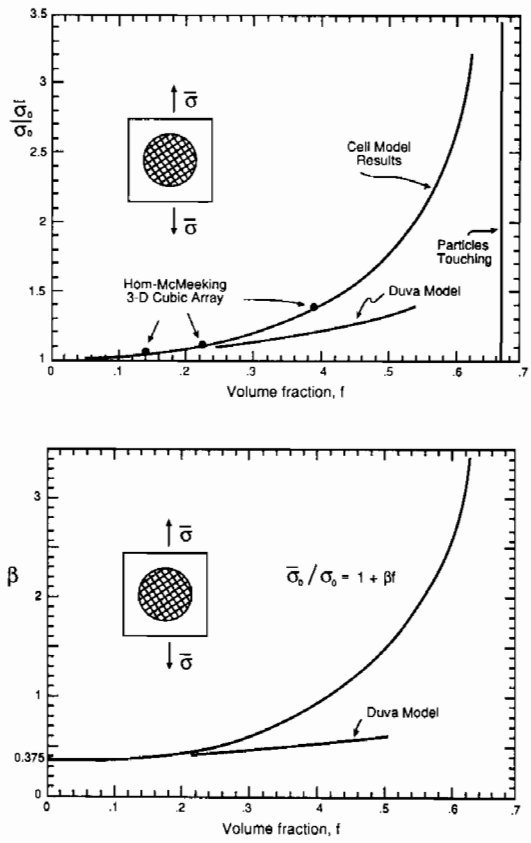

Fig. 4. Limit flow stress as a function of volume fraction for an elastic–perfectly plastic matrix containing rigid spherical particles. The aspect ratio of the cell was taken to be unity.

3. ELASTIC–PERFECTLY PLASTIC MATRIX REINFORCED BY ALIGNED ELLIPSOIDAL PARTICLES

The effect of particle aspect ratio on the composite stress–strain curve is shown in Fig. 5. The rigid particles are ellipsoids of revolution with radius a and half-height b with the axis of revolution aligned with the axis of the cylindrical cell. The particle volume fraction for each curve displayed in Fig. 5 is $f = 0.2$. The cell aspect ratio in each of these calculations is taken to be the same as that of the particle, i.e. $R/H = a/b$. High aspect ratio *needles* ($a/b \ll 1$) or *discs* ($a/b \gg 1$) are far more effective reinforcements than spheres, as is well known. At a given aspect ratio, aligned needles are somewhat more effective than aligned discs. Figure 5 reveals a general trend: the more effective the reinforcement in elevating the matrix flow stress, the larger the strain range associated with the transition.

The normalized limit flow stress, $\bar{\sigma}_0/\sigma_0$, is shown as a function of particle volume fraction in Fig. 6(a) for several values of particle aspect ratio. The β-factor defined in (10) is shown in Fig. 6(b), where the strong dependence of this factor on the particle aspect ratio is evident. At low fractions, aligned needle-shaped particles with an aspect ratio $a/b = 0.1$ are more than ten times as effective as spheres. The range of validity of the dilute approximation [i.e. (10) with β *fixed* at its value for $f = 0$] diminishes as the aspect ratio becomes either large or small. A simple expression for β which accurately reproduces the results of Fig. 6(b) at $f = 0.1$ is

$$\beta \cong 0.69\frac{b}{a} + 0.44\frac{a}{b} - 0.75. \tag{12}$$

The use of this formula for β in conjunction with (10) gives a reasonable approximation for $\bar{\sigma}_0/\sigma_0$ for aligned ellipsoidal particles for $f \leqslant 0.2$.

The effect of the cell aspect ratio R/H on $\bar{\sigma}_0/\sigma_0$ at a *fixed* particle volume fraction ($f = 0.05$) is shown in Fig. 7 for a spherical particle, a needle-shaped particle ($a/b = 0.2$), and a disc-shaped particle ($a/b = 5$). Particularly for the sphere and disc-shaped particles, the composite flow stress remains virtually unchanged over a fairly wide range of the cell aspect ratio. Only as the distance between the particle and the side or ends of the cylindrical cell becomes small does $\bar{\sigma}_0/\sigma_0$ increase rapidly. In the limit when the side or ends of the cell touch the particle, $\bar{\sigma}_0/\sigma_0$ is

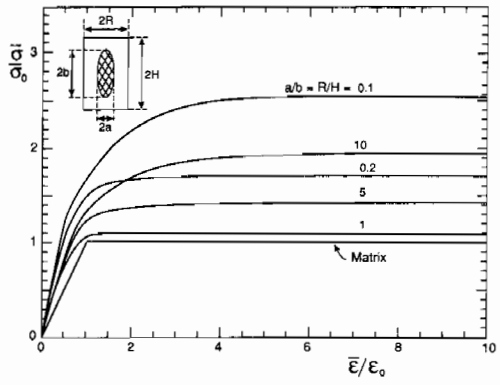

Fig. 5. Uniaxial stress–strain curves for an elastic–perfectly plastic matrix containing aligned ellipsoidal particles of various aspect ratios ranging from needles to spheres to discs. The volume fraction in each case is $f = 0.2$, and the cell aspect ratio was taken to be the same as the particle aspect ratio.

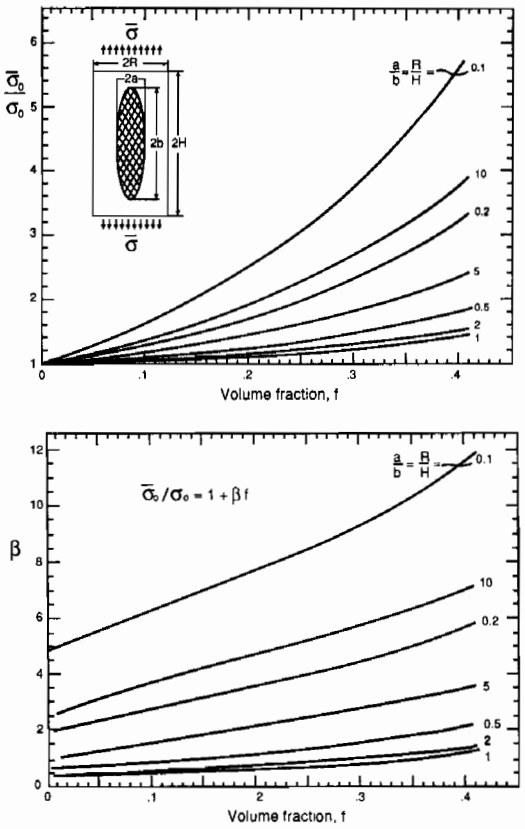

Fig. 6. Limit flow stress as a function of volume fraction for an elastic–perfectly plastic matrix reinforced by aligned ellipsoidal particles.

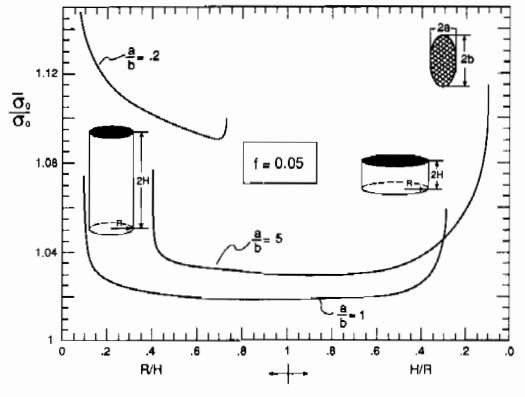

Fig. 7. Effect of cell aspect ratio on the limit flow stress of an elastic–perfectly plastic matrix reinforced by aligned needles ($a/b = 0.2$), discs ($a/b = 5$) and spheres ($a/b = 1$), in each case for $f = 0.05$.

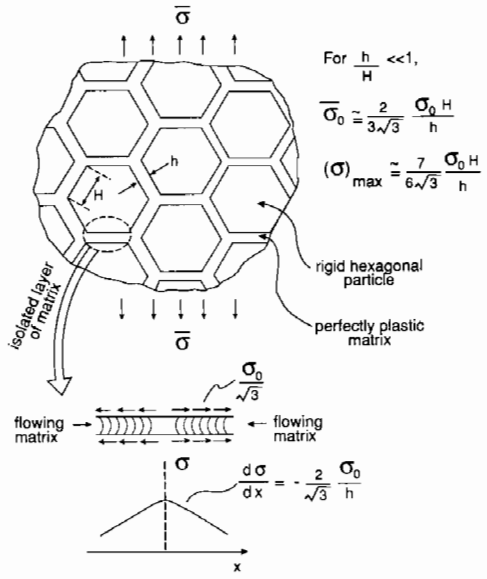

Fig. 8. Synopsis of Drucker's 2D model [9] of a uniform array of rigid hexagonal particles separated by an elastic–perfectly plastic matrix.

unbounded. High stress triaxiality develops in the narrow zones where particles are closed together, as described by Drucker [9] and as emphasized by Christman *et al.* [1].

Drucker's [9] plane strain model of a perfectly plastic matrix reinforced by a high volume fraction of uniformly distributed, rigid hexagonal particles is summarized in Fig. 8. In the limit state, steep gradients of stress develop in the matrix which are inversely proportional to the separation between the particles. This leads to mean stress levels which can be many times the matrix flow stress σ_0. The limit flow stress of the composite is also inversely proportional to the separation between the particles when that distance is small compared to the particle size. The high mean stress which develops in a heavily reinforced composite when overall flow takes place has clear implications for the susceptibility of these materials to various fracture mechanisms.

The limit flow stress $\bar{\sigma}_0$ of a heavily reinforced matrix is a strong function of the arrangement of the particles, especially when they are aligned. The results for the needle-shaped particles ($a/b = 0.2$) in Fig. 7 already suggest such a sensitivity. A number of investigators [1, 2, 4, 5] have shown that the arrangement of needle-shaped particles modeled by the cell used here has a higher flow stress $\bar{\sigma}_0$ than arrangements where the needles are still aligned but overlap one another. The results for high aspect ratio needles or discs are also much more sensitive to the cell aspect ratio than are the results for spherical particles. Effects of arrangement and distribution are important features of the subject which are not yet well understood, as will be emphasized again in the final discussion.

4. ELASTIC–PERFECTLY PLASTIC MATRIX WITH ALIGNED CYLINDRICAL PARTICLES

The work of Christman *et al.* [1] has revealed a strong dependence of the composite flow stress on details of particle shape other than just the aspect ratio. Specifically, they have shown that a uniform distribution of aligned cylindrical particles, whose diameter equals their height, are far more effective reinforcing agents than spherical particles. The results of Fig. 9 compared with those of Fig. 6 for ellipsoidal particles drive this point home. The results for rigid circular cylindrical particles in Fig. 9 have been computed using a cylindrical cell with aspect ratio, R/H, equal to the radius to half-height ratio, a/b, of the particle. At low volume fractions the unit cylindrical particles ($a/b = 1$) are approximately twice as effective as spherical particles at the same volume fraction (i.e. $\beta \cong 0.70$ vs $\beta \cong 0.38$). The volume of the smallest sphere which circumscribes the unit cylinder is 1.89 times that of the unit cylinder, and this factor corresponds very closely to the difference in the β-factors. In other words, the unit cylinder has almost the same effect as a spherical particle whose surface just circumscribes the cylinder.†

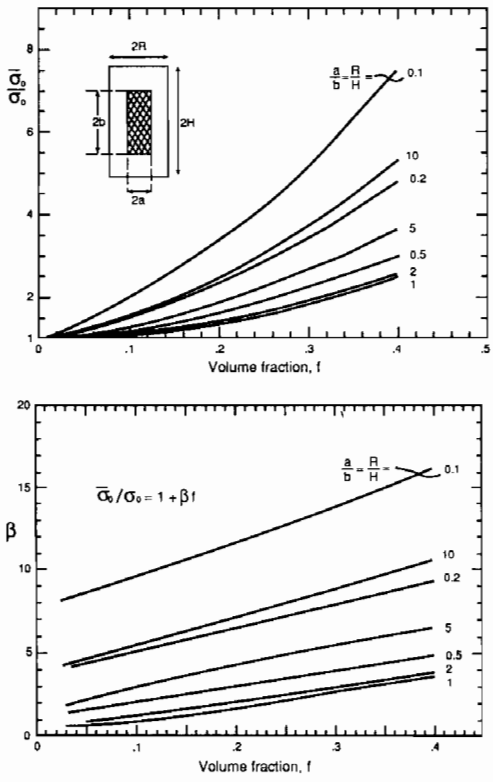

Fig. 9. Limit flow stress as a function of volume fraction for an elastic–perfectly plastic matrix reinforced by aligned cylindrical particles. Compare with the corresponding curves in Fig. 6 aligned ellipsoidal particles.

†The result for the circumscribing spherical particle must be an *upper bound* to $\bar{\sigma}_0$ for the unit cylinder since the velocity field for the spherical particle is admissible for the unit cylinder.

At higher aspect ratios, corresponding to needles or discs, the difference between the effect of cylindrical-shaped particles and the ellipsoidal particles is less dramatic but, nevertheless, still appreciable. At $f = 0.1$, the following provides an accurate approximation to β for the aligned cylindrical particles in Fig. 9(b)

$$\beta \cong 1.06\frac{b}{a} + 0.64\frac{a}{b} - 0.95. \tag{13}$$

This result in (10) provides an approximation to $\bar{\sigma}_0/\sigma_0$ for aligned cylindrical particles in the range $f \leqslant 0.2$.

5. REINFORCEMENT OF MATRICES WHICH UNDERGO POWER-LAW STRAIN HARDENING OR POWER-LAW CREEP

In this section attention is directed to matrices which undergo isotropic hardening in accord with a Ramberg–Osgood tensile stress–strain curve (2). The asymptotic reference stress $\bar{\sigma}_N$ in (3) applies to the rate-independent flow problem and to the steady-state power-law creep problem, as discussed in connection with (5) and (6).

The effect of strain hardening on the full uniaxial stress–strain curve of the composite is shown in Figs 10, 11 and 12. These curves were computed for rigid *cylindrical* particles within a cell whose aspect ratio, R/H, is taken to be equal to that of the particle, a/b. Curves for three aspect ratios are shown, in each case for $f = 0.2$ and $N = 0$, 0.1 and 0.2. The value of α in (2) has been taken to be 3/7, as recommended in [3]; the matrix curves are shown in Fig. 11.

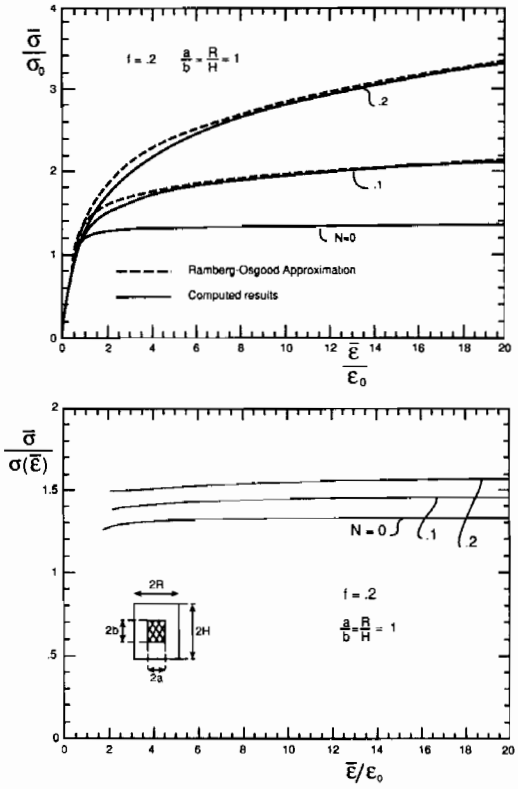

Fig. 10. Tensile stress–strain curve for a matrix material with a Ramberg–Osgood stress–strain curve (see Fig. 11) reinforced by cylindrical particles with unit aspect ratio and $f = 0.2$. The approximation is given by (14). The lower plot shows the overall stress normalized by the stress in the unreinforced matrix at the same strain. $N = 1/n$.

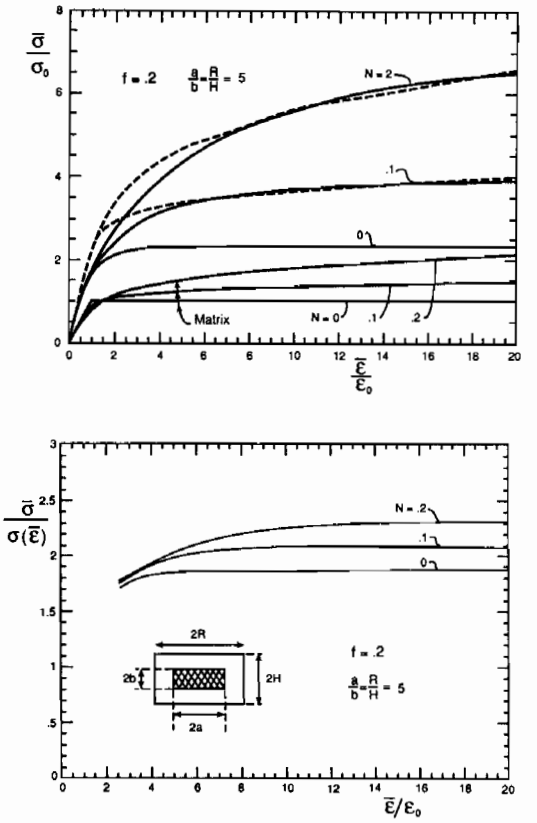

Fig. 11. Tensile stress–strain curve for a matrix material with a Ramberg–Osgood stress–strain curve reinforced by aligned cylindrical discs ($a/b = 5$) with $f = 0.2$. The approximation is given by (14). The lower plot shows the overall stress normalized by the stress in the unreinforced matrix at the same strain. $N = 1/n$.

In part (b) of each of the three figures, the stress $\bar{\sigma}$ has been normalized by the stress of the unreinforced matrix material at the same strain, $\sigma(\bar{\epsilon})$. As discussed in connection with Fig. 1, the normalized composite stress–strain curve is useful in revealing the asymptotic reference stress $\bar{\sigma}_N$ for the power-law material. These normalized plots also give an indication of the length of the *transition* to pure power-law behavior. The transition strain is a function of the level of reinforcement and the degree of strain hardening. It has already been noted that the transition strain for a composite with an elastic–perfectly plastic matrix is typically about $3\epsilon_0$, for moderately high levels of reinforcement. Strain hardening *increases* the transition to as much as $10\epsilon_0$ at high levels of reinforcement with $N = 0.2$ (see Fig. 12).

By similar reasoning, one expects the transient response in creep prior to the attainment of

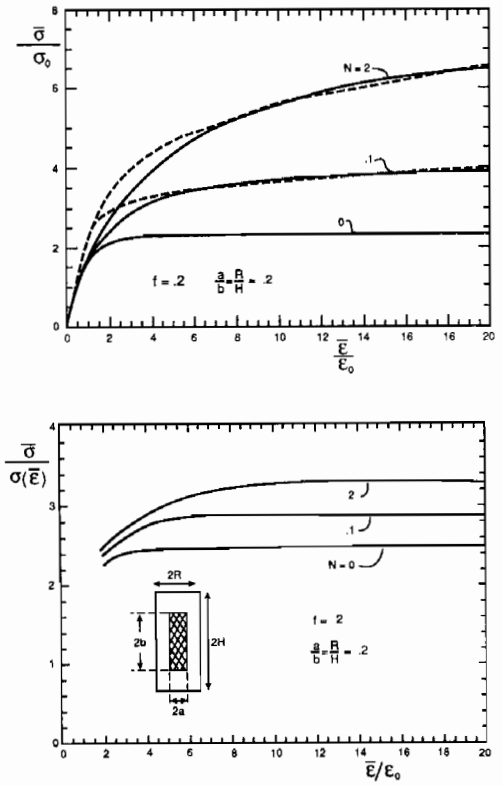

Fig. 12. Tensile stress–strain curve for a matrix material with a Ramberg–Osgood stress–strain curve reinforced by aligned cylindrical needles ($a/b = 0.2$) with $f = 0.2$.

steady-state to involve a transition strain typical of that for the rate-independent composite. The significance of the extended transition for highly reinforced materials with appreciable hardening (or values of N as large as 0.2 in power-law creep applications) is that the transition may constitute a substantial portion of the useable strain range of the composite. Concomitantly, the composite may appear to harden with a different N-value than the matrix if the strain range sampled falls within the transition. An illustration of this point is provided in § 4 of [1] where a difference between the matrix and composite N-values was found. We believe this difference is due to the fact that most of the strain measured (and computed) for the composite considered fell within the transition.

The dashed curves in Figs 10–12 are a Ramberg–Osgood representation for the composite specified as follows. With $\bar{E}$ and $\bar{\sigma}_N$ as the modulus and asymptotic reference stress for the composite, consider the counterpart to (2a) for the composite,

$$\bar{\epsilon} = \frac{\bar{\sigma}}{\bar{E}} + \alpha\epsilon_0 \left(\frac{\bar{\sigma}}{\bar{\sigma}_N}\right)^n. \tag{14}$$

This approximation has the correct behavior in the linear range and has the correct asymptotic pure power-law behavior noted in (3). It can be seen in Figs 10–12 that this approximation is a fairly successful representation for the entire stress–strain curve, although it overestimates the proportional limit and the stress in the transition region. The effect of the elasticity of the particles can be accounted for in $\bar{E}$ in (14).

The details of the composite stress–strain curve in the transition will depend on the details of the matrix stress–strain curve in the vicinity of ϵ_0. The calculations of Figs 10–12 have all been repeated for a piecewise power-law governing the matrix behavior, i.e.

$$\begin{aligned} \epsilon &= \sigma/E \qquad \sigma \leqslant \sigma_0 \\ &= \epsilon_0(\sigma/\sigma_0)^n \quad \sigma > \sigma_0 \end{aligned} \tag{15}$$

where, again, $\epsilon_0 = \sigma_0/E$. The values of the asymptotic reference stress $\bar{\sigma}_N$ coincide with those calculated using the Ramberg–Osgood curve, as they must. Moreover, the piecewise power-law representation for the composite

$$\begin{aligned} \bar{\epsilon} &= \bar{\sigma}/\bar{E} \qquad \bar{\sigma} \leqslant \bar{\sigma}_* \\ &= \epsilon_0(\bar{\sigma}/\bar{\sigma}_N)^n \quad \bar{\sigma} > \bar{\sigma}_* \end{aligned} \tag{16}$$

where $\bar{\sigma}_* = \bar{\sigma}_N\ (\bar{\sigma}/\bar{\sigma}_N)^{1/(n-1)}$, provides a reasonable approximation to the computed results over the entire strain range. This representation is not quite as successful as the Ramberg–Osgood representation since it has a discontinuity in slope at $\bar{\sigma}_*$ which is not present in the computed results for the composite. As in the other case, it overestimates the stress in the transition.

The asymptotic reference stress $\bar{\sigma}_N$ of the composite with a hardening matrix is larger than the corresponding quantity, $\bar{\sigma}_0$, for the composite with an elastic–perfectly plastic matrix, as can be seen in lower halves of Figs 10–12. A plot of $\bar{\sigma}_N - \bar{\sigma}_0$ normalized by $\bar{\sigma}_0 - \sigma_0$ as a function of N is shown in Fig. 13. Included in this figure are results for aligned cylindrical particles ranging from discs to spheres to needles at two volume fractions. Also included are predictions of the Duva model for spherical particle reinforcement which is given below. The increase in $\bar{\sigma}_N$ above $\bar{\sigma}_0$ is nearly linear in N. For the more heavily reinforced materials (containing disc- or needle-shaped particles), the approximation, $(\bar{\sigma}_N - \bar{\sigma}_0)/(\bar{\sigma}_0 - \sigma_0) \cong 2.5\,N$, holds, so that

$$\bar{\sigma}_N \cong \bar{\sigma}_0 + 2.5\,N(\bar{\sigma}_0 - \sigma_0). \tag{17}$$

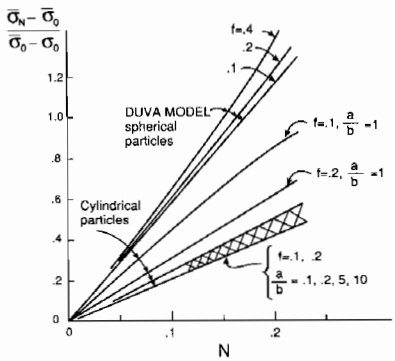

Fig. 13. Increase of asymptotic reference stress $\bar{\sigma}_N$ above $\bar{\sigma}_0$ as a function of N for various reinforcements.

The details of the structure of the composite (i.e. f, aspect ratio, etc.) are all contained in $\bar{\sigma}_0 - \sigma_0$ in this approximate formula. For equiaxed particles the coefficient in (17) is closer to 3.5 than 2.5.

Duva's [8] differential self-consistent result for the reference stress of a composite with a random distribution of rigid spherical particles perfectly bonded in a pure power-law matrix is

$$\bar{\sigma}_N = \sigma_0(1-f)^{-h(N)} \tag{18}$$

where

$$h(N) \cong 0.39(1-N)+\tfrac{5}{2}N. \tag{19}$$

The function of the hardening exponent, $h(N)$, has been obtained from the solution to the problem of an isolated spherical particle in an infinite pure power-law matrix. Duva's numerical solution gave $h(N) \cong 0.48\ (1-N)+\frac{5}{2}N$. The result quoted in (19) and used in (9) was recomputed in the present study using a more accurate numerical procedure. The recomputation was carried out for the elastic-perfectly plastic limit, $N=0$, using the procedure described in [10] which employs a series of functions to represent the velocity field in the matrix. The calculations in [8] and [10] used only two free amplitude factors in the calculation procedure. The calculations were repeated in the present study by systematically increasing the number of amplitudes of the functions to 35, giving $h(0)=0.39$. The approximately linear dependence of h on N was suggested by the results in [8] and was retained in (19).

The Duva model is formulated such that the dilute limit is exact. From (18)

$$\bar{\sigma}_N/\sigma_0 = 1 + h(N)f \tag{20}$$

for sufficiently small f. From the plots in Fig. 4, it can be seen that Duva's model significantly underestimates strengthening at non-dilute concentrations of particles.

6. LIMIT YIELD SURFACE OF COMPOSITES WITH ALIGNED PARTICLES SUBJECT TO MULTIAXIAL STRESS STATES

A study has been conducted to determine the limit yield surface of the elastic–perfectly plastic matrix reinforced by aligned disc-shaped particles. A three dimensional cell has been used as shown in the insert in Fig. 14. the rectangular box-shaped cell contains a centered, rigid particle in the form of an ellipsoid of revolution. As in Fig. 2, the cell is imagined to be one unit of an array of identical units repeated in all three directions. Under overall stressing in the 1- and 2-directions, the sides of the cell remain planar and do not rotate. Shear stresses vanish on the cell sides and the average normal tractions equal $\bar{\sigma}_{11}$, $\bar{\sigma}_{22}$ and $\bar{\sigma}_{33}=0$, respectively.

Plots of the limit yield stress as a function of particle volume fraction are shown in Fig. 14 for uniaxial tension in the 1-direction and in the 2-direction. The particles are discs (ellipsoids with $a/b=10$). The aspect ratio of the box cell was chosen such that the area of the cross-section of the cell perpendicular to the x_1-direction was the same as that used in the corresponding axisymmetric cell model, i.e. $4L^2=\pi R^2$. Thus, since $R/H=10$ was used for the axisymmetric cell, $L/H=8.862$ was chosen for the 3D box cell. With this choice, the limit yield stress for stress in the x_1-direction calculated using the 3D formulation agreed to within 1% of the values calculated using the axisymmetric cell for the range $f \leqslant 0.4$. The 3D calculations were carried out using a 20-node quadratic brick element. For a typical 3D mesh, 688 elements were used. The strain increment was taken to be $\Delta\epsilon/\epsilon_0=0.125$ and thus 80 increments were needed to complete a typical stress–strain curve for overall strains up to $10\,\epsilon_0$.

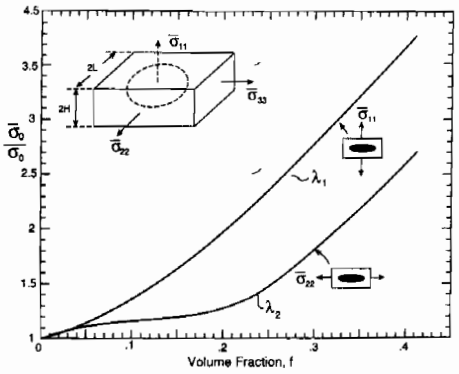

Fig. 14. Limit flow stress for uniaxial stressing in two directions for aligned ellipsoidal discs ($a/b=10$) in an elastic–perfectly plastic matrix.

The tensile flow stress enhancement in the direction of alignment substantially exceeds that in the transverse direction. For stressing in the 1-direction the overall strain rates necessarily satisfy $\dot{\bar{\epsilon}}_{22}=\dot{\bar{\epsilon}}_{33}=-\frac{1}{2}\dot{\bar{\epsilon}}_{11}$. For stressing in the 2-direction with $f \geqslant 0.2$, the overall straining in the limit state is almost entirely in the (2, 3) plane (i.e. $\dot{\bar{\epsilon}}_{11} \cong 0$ and $\dot{\bar{\epsilon}}_{33} \cong -\dot{\bar{\epsilon}}_{22}$), reflecting the anisotropy associated with the reinforcement.

The limit yield surface of the composite for all combinations of $\bar{\sigma}_{11}$ and $\bar{\sigma}_{22}$ with $\bar{\sigma}_{33}=0$ has been computed using the 3D box cell for the same disc-like reinforcements ($a/b=10$) for $f=0.2$. This computed surface is shown in Fig. 15 along with the prediction from a phenomenological yield surface which is chosen to reproduce the intercepts at $\bar{\sigma}_{11}=0$ and $\bar{\sigma}_{22}=0$. The phenomenological yield surface is now introduced.

With x_i-axes defined as in the insert in Fig. 14, we will require the phenomenological limit yield surface of the composite to be transversely isotropic with respect to the x_1-axis. It is required to be independent of $\bar{\sigma}_{kk}$. For uniaxial tension in the 1-direction require $\bar{\sigma}_{11}=\lambda_1\,\sigma_0$, and for uniaxial tension in the 2-direction require $\bar{\sigma}_{22}=\lambda_2\,\sigma_0$. In addition, it will be assumed that the disc-like reinforcements have no effect on the

overall yield stress under a pure shear stress $\bar{\sigma}_{12}$ (or $\bar{\sigma}_{13}$). Thus in pure shear $\bar{\sigma}_{12} = \sigma_0/\sqrt{3}$.

The limit yield surface which is a quadratic function of the stress components and which satisfies the above requirements is

$$(\bar{\sigma}_{11}/\lambda_1)^2 + (\bar{\sigma}_{22}/\lambda_2)^2 + (\bar{\sigma}_{33}/\lambda_2)^2 + (\lambda_1^{-2} - 2\lambda_2^{-2})\,\bar{\sigma}_{22}\bar{\sigma}_{33} - \lambda_1^{-2}\bar{\sigma}_{11}(\bar{\sigma}_{22} + \bar{\sigma}_{33}) + 3(\bar{\sigma}_{12}^2 + \bar{\sigma}_{13}^2) + (4\lambda_2^{-2} - \lambda_1^{-2})\bar{\sigma}_{23} = \sigma_0^2. \quad (21)$$

This reduces to the Mises surface when $\lambda_1 = \lambda_2 = 1$.

The quadratic yield surface (21) can also be used to approximate the yield surface of the composite when the reinforcements are needle-like particles aligned with the x_1-axis, since the requirements stipulated above continue to apply. Now, λ_1 and λ_2 must be obtained from calculations for the needle-like particles. It is again true that yield under pure shear $\bar{\sigma}_{12}$ is hardly influenced by the reinforcement. Dvorak and Bahei-El-Din [11] have discussed features of the overall yield surface of fiber reinforced composites which are analogous to those seen in Fig. 15.

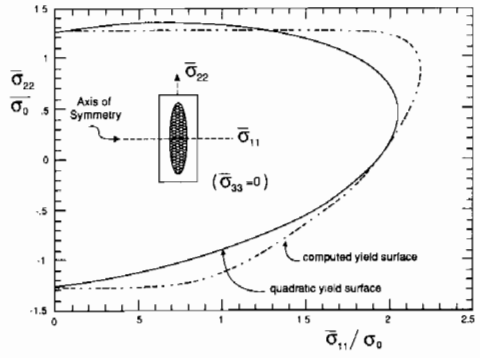

Fig. 15. Limit yield surface for combinations of $\bar{\sigma}_{11}$ and $\bar{\sigma}_{22}$ for an elastic–perfectly plastic matrix reinforced by aligned ellipsoidal discs ($a/b = 10$) with $f = 0.2$. The quadratic yield surface is specified by (21).

7. ESTIMATES OF THE TENSILE FLOW STRESS OF AN ELASTIC–PERFECTLY PLASTIC MATRIX REINFORCED BY RANDOMLY ORIENTATED PACKETS OF DISC-LIKE OR NEEDLE-LIKE PARTICLES

In this section the approximate yield surface (21) for aligned particles is exploited to obtain an estimate for the limit tensile flow stress of a composite with randomly orientated particles. Specifically, morphologies are considered for relatively high density, high aspect ratio reinforcements wherein particles are aligned in grain-like "packets" as depicted in Fig. 16. High aspect ratio, mono-sized disc-like particles must be in a packet morphology if they are packed to even modest volume fractions. Needles need not have such a morphology, but the packet morphology does occur for certain systems [13].

We consider a composite with randomly oriented packets where the yield behavior of each packet is controlled by (21). A uniform strain rate upper bound

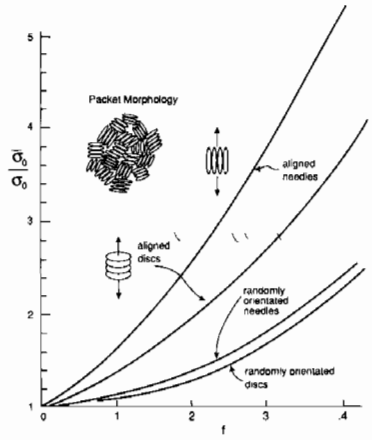

Fig. 16. Uniaxial limit flow stress for aligned and randomly oriented ellipsoidal needles ($a/b = 0.1$) and discs ($a/b = 10$) in an elastic–perfectly plastic matrix. The randomly oriented particles are assumed to possess a packet-like morphology.

to the limit tensile flow stress of this composite is readily computed. The calculation is directly analogous to the Taylor/Bishop–Hill [12] upper bound to the tensile flow stress of polycrystals with randomly oriented single crystals. In what follows, a brief description of the calculation procedure is given along with one set of results for disc- and needle-shaped particles. A more detailed description and study will be reported in a subsequent publication.

To obtain an upper bound to the limit tensile flow stress $\bar{\sigma}_0$ of the composite, impose the same uniform strain rate on all packets where in the specimen axes

$$\dot{\epsilon}_{11} \equiv \dot{\bar{\epsilon}}, \quad \dot{\epsilon}_{22} = \dot{\epsilon}_{33} = -\tfrac{1}{2}\dot{\bar{\epsilon}}, \quad \dot{\epsilon}_{12} = \dot{\epsilon}_{13} = \dot{\epsilon}_{23} = 0. \quad (22)$$

With $\dot{\epsilon}'_{ij}$ denoting the strain rate components in the axes of transverse isotropy of a given packet (say, with the 1′-axis aligned with the axis of transverse isotropy), let s'_{ij} be the deviator stress associated with $\dot{\epsilon}'_{ij}$ by normality to (21). That is, with $f(\boldsymbol{\sigma}') = \sigma_0^2$ denoting (21), s'_{ij} is obtained by solving

$$\dot{\epsilon}'_{ij} = \dot{\mu}\frac{\partial f(\boldsymbol{\sigma}')}{\partial s'_{ij}} \qquad (\dot{\mu} > 0) \quad (23)$$

subject to (21) itself. The solution s'_{ij} can be obtained explicitly but will not be displayed.

The upper bound $\bar{\sigma}_0$ is obtained from

$$\bar{\sigma}_0 = (\dot{\bar{\epsilon}})^{-1}\int s'_{ij}\dot{\epsilon}'_{ij} \quad (24)$$

where the integral represents an equally weighted average over all orientations of the packet axes relative to the specimen axes. Because the packet has transverse isotropy, the integration in (24) can be reduced to a single integral over the Euler angle between the 1′-axis of the packet and the specimen tensile axis. This integration has been carried out using straight forward numerical procedures. The final result has the form

$$\bar{\sigma}_0 = \sigma_0 F(\lambda_1, \lambda_2). \quad (25)$$

The results of the calculations are shown in Fig. 16 for composites with packets of discs (ellipsoids with $a/b = 10$) and needles ($a/b = 1/10$). For comparison, the limit flow stresses for the composites with the same aligned discs or needles are also shown. For the disc-shaped particles the values of λ_1 and λ_2 are those given in Fig. 14. For the needle-shaped particles, λ_1 is obtained as $\bar{\sigma}_0/\sigma_0$ from Fig. 6(a). (This is the same curve plotted for the aligned needles in Fig. 16.) Three dimensional calculations for λ_2 have not yet been carried out for the needle-shaped particles. The rough estimate $\lambda_2 = 1 + 0.5f$ has been used based on 2D plane strain results which are available. Repeating the calculation with $\lambda_2 = 1$ gives only slightly lower results for the needle-shaped particles. The appreciable advantage of aligned needle-shaped particles over aligned disc-shaped particles seen in Fig. 16 is lost when the particles are randomly distributed in the packet morphology because λ_2 for the discs is much larger than for the needles.

The randomly oriented discs have a very similar reinforcing effect on the elastic–perfectly plastic matrix as the needles in the packet morphology. Note from Fig. 9 that the aligned unit cylinders also have a comparable reinforcing effect to the randomly oriented discs and needs in Fig. 16. Presumably the transverse limit yield stress for the aligned unit cylinders is not too different from the results in Fig. 9. Thus it appears that a fairly wide range of particle shapes has roughly the same effect on the elastic–perfectly plastic matrix when the particles have random orientation. A similar conclusion concerning the initial yield behavior was reached by Brown and Clark [16].

8. CONCLUDING DISCUSSION

The assumption underlying the use of continuum plasticity to predict particle strengthening of ductile matrix materials is the existence of a very small length characterizing the dislocation structure compared with the size and spacing of the particles. A clear cut rule for when these conditions can be expected is not available, and no doubt may be a strong function of the matrix material itself and possibly on whether the application is to rate-independent plastic flow or to high temperature creep. The continuum theory results presented in the body of this paper do not depend on the absolute size of the particles. The absence of a significant size effect is consistent with some stress–strain data on SiC particle reinforced aluminum matrix composites [13, 14] with particles ranging in size from 10 to 165 μm but apparently not with other data [15] for particles in the same size range. Literature related to the current status of the issue is cited in [2].

The arrangement of aligned fibers in a uniform array has been shown to be important in [1, 2, 4, 5]. The strengthening resulting from overlapping fibers is less than that achieved by non-overlapping fibers modeled by the cell configuration employed in this paper. In general, arrangement appears to play a more important role in the nonlinear response of composites than in the linear behavior, but the subject is relatively unexplored. Even less studied are the plastic properties of composites with randomly oriented fibers or discs. The bounding method of Section 7 has potential when a packet morphology allows the use of results from aligned particles to be used to characterize yield within sub-regions of the composite. The two examples in Fig. 16 emphasize that the high strengthening due to *aligned* high aspect ratio particles is not achieved when the orientation of the particles is randomly distributed. Whether this holds true for other morphologies of randomly oriented fibers remains to be seen.

Given a matrix with either a Ramberg–Osgood tensile curve or a piecewise power-law curve, equation (14) or (16) provides an approximation to the uniaxial stress–strain curve of the composite in terms of just two quantities, the overall elastic modulus, $\bar{E}$ and $\bar{\sigma}_N$. Strain hardening of the matrix is magnified by the particulate reinforcements. This is evident in Figs 10–12 and is perhaps most transparent in the approximate relation (17) between the asymptotic reference stress $\bar{\sigma}_N$ and the strain hardening exponent N. The greater is the reinforcement of the elastic–perfectly plastic matrix as measured by $\bar{\sigma}_0 - \sigma_0$, the greater is $\bar{\sigma}_N - \bar{\sigma}_0$.

Acknowledgements—The authors acknowledge interaction with A. G. Evans throughout the work. This work was supported in part by the DARPA University Research Initiative (Sub-agreement P.O. No. VB38639-0 with the University of California, Santa Barbara, ONR Prime Contract N00014-86-K0753). The work of JWH was supported additionally by NSF grant MSM-88-12779 and by UCSB and Harvard University. Provision of the ABAQUS finite element code by Hibbitt, Karlsson and Sorensen Inc. of Providence, R.I. is gratefully acknowledged. The calculations on the FPS 500EA computer were made possible by FPS Computing through the UCSB Industrial Liaison Program.

REFERENCES

1. T. Christman, A. Needleman and S. Suresh, *Acta metall.* **37,** 3029 (1989) (see also a corrigendum to be published in *Acta metall. mater.*).
2. J. M. Papazian and P. N. Adler, Part I, *Metall. Trans. A* **21A,** 401 (1990); A. Levy and J. M. Papazian, Part 2, *Metall. Trans. A* **21A,** (1990).
3. W. Ramberg and W. R. Osgood, NACA TN 902 (1943).
4. V. Tvergaard, *Acta metall. mater.* **38,** 192 (1990).
5. T. L. Dragone and W. D. Nix, *Proc. TMS Int. Conf. on Advanced Metal and Ceramic Composites*, Anaheim, Calif. (1990).
6. J. P. Watt, G. F. Davies and R. J. O'Connell *Rev. Geophys. Space Phys.* **14,** 541 (1976).
7. C. L. Hom and R. M. McMeeking, *Int. J. Plasticity*. To be published.
8. J. M. Duva, *Trans. ASME Series H, J. Engng Mater. Technol.* **106,** 317 (1984).

9. D. C. Drucker, in *High Strength Materials* (edited by V. Zakay), p. 795. Wiley, New York (1965).
10. N. A. Fleck, J. W. Hutchinson and V. Tvergaard, *J. Mech. Phys. Solids* **37,** 515 (1989).
11. G. J. Dvorak and Y. A. Bahei-El-Din, *Acta mechanica* **69,** 219 (1987).
12. J. F. W. Bishop and R. Hill, *Phil. Mag.* **42,** 414, 1298 (1951).
13. Y. Yang, C. Cadȳ, M. S. Hu, F. Zok, R. Mehrabian and A. G. Evans, *Acta metall. mater.* **38,** 2613 (1990).
14. Y. Yang, S. Pickard, C. Cady, A. G. Evans and R. Mehrabian, *Acta metall. mater.* **39,** 1863 (1991).
15. S. V. Karnat, J. P. Hirth and R. Mehrabian, *Acta metall.* **37,** 2395 (1989).
16. L. M. Brown and D. R. Clarke, *Acta metall.* **23,** 821 (1975).